

Advanced Materials Research Vol. 136

# Frontier in Functional Manufacturing Technologies

Edited by  
Dunwen Zuo, Hun Guo, Hongli Xu, Chun Su,  
Chunjie Liu and Weidong Jin

# **Frontier in Functional Manufacturing Technologies**

Edited by  
Dunwen Zuo  
Hun Guo  
Hongli Xu  
Chun Su  
Chunjie Liu  
Weidong Jin

# **Frontier in Functional Manufacturing Technologies**

Selected, peer reviewed papers from the  
2nd International Conference on Functional Manufacturing Technologies  
(ICFMT 2010),  
Aug.6-9 2010, Harbin, Heilongjiang, China

*Edited by*

**Dunwen Zuo, Hun Guo, Hongli Xu, Chun Su,  
Chunjie Liu and Weidong Jin**



**TRANS TECH PUBLICATIONS LTD**  
**Switzerland • UK • USA**

**Copyright** © 2010 Trans Tech Publications Ltd, Switzerland

All rights reserved. No part of the contents of this publication may be reproduced or transmitted in any form or by any means without the written permission of the publisher.

Trans Tech Publications Ltd  
Laubisrutistr. 24  
CH-8712 Stafa-Zurich  
Switzerland  
<http://www.ttp.net>

Volume 136 of  
*Advanced Materials Research*  
ISSN 1022-6680

Full text available online at <http://www.scientific.net>

***Distributed worldwide by***

Trans Tech Publications Ltd  
Laubisrutistr. 24  
CH-8712 Stafa-Zurich  
Switzerland

Fax: +41 (44) 922 10 33  
e-mail: [sales@ttp.net](mailto:sales@ttp.net)

***and in the Americas by***

Trans Tech Publications Inc.  
PO Box 699, May Street  
Enfield, NH 03748  
USA

Phone: +1 (603) 632-7377  
Fax: +1 (603) 632-5611  
e-mail: [sales-usa@ttp.net](mailto:sales-usa@ttp.net)

# PREFACE

It is fundamental to prosper the country. With the increasingly pressure of world population, resource, environment and so on today, Chinese manufacture corporations, especially equipment manufactures, encounter severe challenge. Functional Manufacturing Technologies, as a nuclear part of equipment manufactures being developed greatly, are playing a more and more important role.

The special volumes are to communicate the latest progress and research results of new theory, new technology, method, equipment and so on in advanced manufacturing technology field, and to grasp the updated technological and research trends in international, which will drive international communication and cooperation of production, education and research in this field.

The major topics covered by the special volumes include Anti-fatigue Design and Anti-fatigue Manufacturing, Manufacturing System and Reliability, Processing detection and monitoring-controlling, CIMS and management system, Production system mould and Simulation technology, Quality Control of Manufacturing Systems, Agile Manufacturing, Finite Element Analysis and structure optimization, Digital manufacturing and Robotics, Rapid prototyping technology, Reverse engineering technology, High-speed (Ultra high speed) precise cutting technology, Ultra precise processing technology, Micro machining technology, Pattern recognition technology, Image processing technology, Sensor and signal detection technology, Non traditional machining technology, Mine equipment manufacturing and technology, Advanced Manufacturing System and Technologies and so on.

# Table of Contents

## Preface

<b>Effect of Rare Earth Ce on Casting Properties of Al-4.5Cu Alloy</b> S.K. Xie, R.X. Yi, Z. Gao, X. Xia, C.G. Hu and X.Y. Guo	1
<b>Simulation and Experimental Investigations of Fiber Diameter of Spunbonding Nonwovens by Means of the Air Jet Flow Field Model</b> B. Zhao	5
<b>Numerical Simulation of Accumulative Forming Bipolar Plates of Fuel Cell</b> Z.Y. Xu, J.J. Wang, S. Ding, W. Wen, Y. Wang and B.F. Yin	10
<b>Low Temperature Synthesis and Luminescent Properties of Ca<sub>2</sub>SnO<sub>4</sub>: Eu<sup>3</sup></b> Y.Z. Li and X.C. Zhou	14
<b>Study on Load-Velocity Dynamic Property of Piston-Type Hydraulic Cylinder Based on SIMULINK</b> X.S. Jin, S.Y. Ding, X.Z. Tang and Z.X. Hu	18
<b>Study on Formability about ME20M Magnesium Alloy Sheet</b> T.F. Zhang and S.K. Xie	23
<b>Effect of Adding Er on Interfacial Reactions between Sn-3.0Ag-0.5Cu Solder and Cu Substrate</b> H. Li and B. Lu	28
<b>Ocular Aberrations Measurement Combined with Subjective Visual Compensation</b> A.C. Xu, J.B. Chen, P.M. Zhang and J.J. Wu	33
<b>Analysis of the Milling Distortion Due to Residual Stress Based on FEM</b> Y.W. Liu	39
<b>Research of Thermodynamics and Properties of Pb/WC-ZrO<sub>2</sub> Inert Electrodes Used in Zinc Electrodeposition</b> R.D. Xu, J.L. Wang and J.F. Zhou	43
<b>Study on Influence Scope of Shock Wave and Smoke Flow after Gas Explosion</b> Z.M. Qu	48
<b>Fabrication of Biodegradable Polymeric Micro-Analytical Devices Using a Laser Direct Writing Method</b> W.W. Zhang, J.J. Zhu, W.K.C. Yung and S.S. Ang	53
<b>Research on Fabricating Technology of Three Dimensional Integrated Braided Composite I Beam</b> X.Y. Pei and J.L. Li	59
<b>Simulated Annealing Genetic Algorithm and its Application in Mixed-Model Assembly Line Design</b> Y. Jiang, X.F. Li, D.W. Zuo, G.M. Jiao and S.L. Xue	64
<b>Construction of Marketing Management Information System of Travel Agency Based on Customer Relationship Management</b> M. Wei	69
<b>Research on the Application of Fuzzy Neural Network in the Automobile Reliability</b> Y.Z. Men	77
<b>A Multi Agent-Based Approach for Supply Chain Network</b> R. Wang	82
<b>Experiment Research of Cutter Edge and Cutting Parameters Influence on Machined Surface Roughness for High Speed Milling Hardened Steel</b> W. Zhang, M.L. Zheng, M.M. Cheng and Q. Wan	86
<b>Study on Laser Triangulation Measurement Principle of Three Dimensional Surface Roughness</b> F.K. Cui, Z.B. Song, X.Q. Wang, F.S. Zhang and Y. Li	91
<b>Estimation and Display of Triangular Mesh Curvature in Reverse Engineering</b> H.C. Shen, J.J. Nie, W.S. Zong, J. Wang and B.G. Yang	95
<b>The Optimization for Design of the Parameters of Spiral Baffle</b> C.C. Lin and C.C. Kuo	103
<b>Feature Analysis for Milling Force of Three-Edge End Mills</b> C. Liu, G.Y. Tan, G.H. Li, J.S. Liang and D.R. Li	108

<b>The Reliability Analysis of a Vacuum Forming Mold for IC Packing Bag</b> W.S. Lin	114
<b>A Non-Linear Flow Channel Implementation Method in Magnetic Gap Space of Magneto-Rheological Valve</b> C.R. Tang and D.D. Liu	118
<b>The Analysis of Key Influence Factors and Application Countermeasures on Quality of FDM Prototype Model</b> Q.Q. Hou and C. Zhao	122
<b>Calculation Method for the Profile Curves of Cycloidal Pump</b> Y.F. Wu, C.L. Xia and Y.G. Shi	126
<b>Effect of Alkaline Treatment of Wood Flour on Strength of Wood-Plastic Composites for Selective Laser Sintering</b> K.Y. Jiang, Y.L. Guo, W.L. Zeng, Z.S. Xin and X. Liu	131
<b>Application of Regression Analysis of Reliability Research in Off-Center Wearing on Well Tube and Rod of Oil Sucker</b> P. Zhou, X.L. Liu, J. Yao and W. Lu	135
<b>A Modified Wavelet Transform Profilometry</b> C.Y. Liu, B. Zhou and X.M. Zhao	140
<b>Simulation Study on Deep Hole Drilling Machine Hydraulic System Based on System Schematic Diagram</b> H. Cao and W.H. Wu	144
<b>Study on the Green Processing of Impeller</b> M.J. Feng, C.T. Sun, X.F. Wang and H.J. Sun	148
<b>Development of a Ring Permeability Test System</b> Y.H. Du, X.M. Jiang and X.R. Li	153
<b>The Variable Non-Linear Flow Channel Method and Device</b> D.D. Liu and C.R. Tang	158
<b>Research on Bearing Life Prediction Based on Three Parameters Weibull Distribution</b> F.S. Zhang, T.T. Liu, J.T. Liu and F.K. Cui	162
<b>The Study of Target Points Center Extracting and Matching in Calibration</b> B. Zhou, D.P. Wang and J. Yang	167
<b>The Prediction of Shot Peening's Surface Roughness with Premixed Water Jet Based on Neural Network</b> R.H. Wang, C. Wang and X.M. Zhang	172
<b>Research on Safety Protection Technology of Conventional Lathe CA6140</b> W.G. Du, H.Y. Zhong and Y.Y. Guo	176
<b>Preparation and Properties of Waterborne Polyurethane with PDMS Side Chain</b> R.F. Yue and S.C. Li	179
<b>Investigation of the Drawing Process of a Square Rod from a Round Bar by Using 3-D Finite Element Analysis</b> T.S. Yang and S.Y. Chang	184
<b>Finite Element Numerical Simulation of EDM Surface Strengthening in Gas Medium of Stainless Steel 1Cr13</b> H.X. Wang, X. Zhang and W.S. Zhang	189
<b>The Application and Development of Microbubble Column Flotation Technology in China</b> Y.T. Wang	194
<b>Effects of Isothermal Process Parameters on the Microstructure of Semisolid AlSi7Mg Alloy Produced by EPM</b> W.T. Tian and G.A. Zhang	202
<b>Study on Dynamic Fuzzy Classification of Design Proposal Based on Design Style</b> Z. Gao and X.M. Ji	207
<b>Analytical Study on Kinetic Characteristic of the Shell of Air-Powered Diving Pump</b> G.X. Tang	212
<b>Study on Variant Design and Improving Technology of Complex Mechanical Products Based on Knowledge Reuse</b> W.D. Jin and H. Guo	216
<b>Study of Modeling and Distortion Predicting for Multi-Frame Components</b> J. Chen	221

---

<b>The Development of Fault Diagnosis System of Reciprocating Compressor Based on LabVIEW</b>	
J.F. Pei, S.X. Qi and W.Y. He	227
<b>The Dynamic Finite Element Analysis of Table of VM1000 CNC Machining Center</b>	
F.H. Yin	231
<b>Integration Technology and Application Research on Management Information in Textile Industry</b>	
Z.W. Chen, Z.F. Chen and Y. Xu	236
<b>Flexible Wedge-Effect for Insect Flying and Fishtail-Effect for Fish Swimming</b>	
X.Y. Jin, N. Lu, B. Zhang and J.P. Yan	242
<b>Study on Cumulate Function of Cut-In Impacting Disrepair with Waved-Edge Milling Insert</b>	
Z.G. Wang, H.G. Wei, Z.J. Li and D.S. Cai	247
<b>Preparation of V-Doped Titanium-Bearing Blast Furnace Slag and its Antibacterial Activity to Mildew</b>	
H. Wang, H. Yang and X.X. Xue	252
<b>Study on Temperature Field of Different Substrate Shape in Preparing Diamond Film</b>	
D.S. Li, D.W. Zuo, X.L. Zhou and X.Z. Hua	256
<b>Research on Fatigue Behaviors of Nodular Cast Iron QT800 by Laser Shock Processing</b>	
Z.P. Wang	260
<b>Numerical Simulation of Thermal Deformation of High Speed and Exactitude Thermo Grip</b>	
Z.G. Wang, L. Xu, H.G. Wei, L.D. Xu and H.H. Yu	264
<b>FTA-BN Approach to Risk Assessment of Die Casting Die and Risk Mitigation Solution in 4Ps Development Framework</b>	
J.J. Jiang, Y.Q. Zhou and M. Miao	269
<b>Study on Atmospheric Corrosion Behaviour of Sic/Al Composite</b>	
X.L. Zhou, D.S. Li, A.H. Zou, X.Z. Hua, G.Z. Ye, Q.J. Chen, J.Y. Zhang and Y.J. Tang	275
<b>Experiment Research on Grinding of Optical Glass with Indigenously Developed Monolayer Brazed Diamond Grinding Wheel</b>	
B. Zhang, H.J. Xu, Y.C. Fu and H.H. Su	279
<b>Open CNC System Based on Embedded Monitoring Unit</b>	
T.Y. Wang, Z.F. Qiao, Q.J. Liu and M. Hu	284
<b>Study on Adsorption Characteristics of Ni (II) by Palygorskite</b>	
S.H. Lin, J.R. Li, Z. Wang and Z.Q. Jing	289
<b>Experimental Study on Thermostatic Cutting Nickel-Base Superalloy GH4169</b>	
Z.P. Hao, R.D. Han and D. Gao	293
<b>Research on RFID and Vision-Based AGV Navigation</b>	
Z.G. Man, W.H. Ye, P. Zhao, P.H. Lou and T.J. Wu	298
<b>Study on Data Acquisition System for Cold Extrusion of Internal Threads Based on Virtual Instrument</b>	
M. Zhang, X.F. Li, D.W. Zuo and H. Miao	303
<b>The Influence of Surface Tension on Lubrication Film Thickness and Pressure</b>	
J.P. Liu, X.Y. Zhang and Q.X. Jia	307
<b>New Technology of Solospun and Prospect of its Application and Development</b>	
B. Zhao	312
<b>Study of Traction Properties of Three Space Lubricants Used for Rolling Bearing</b>	
J.P. Liu, X.Y. Zhang and Q.X. Jia	316

## Effect of Rare Earth Ce on Casting Properties of Al-4.5Cu Alloy

Xie Shikun<sup>a</sup>, Yi Rongxi<sup>b</sup>, Gao Zhi<sup>c</sup>, Xia Xiang<sup>d</sup>, Hu Chagen<sup>e</sup> and Guo Xiuyan<sup>f</sup>

School of Engineering, Jinggangshan University, Ji'an, 343009, PR China;

<sup>a</sup>xskun@163.com, <sup>b</sup>yirongxi@sina.com, <sup>c</sup>gaozhi03@21cn.com, <sup>d</sup>xiax1117@163.com,  
<sup>e</sup>htr\_ly@126.com, <sup>f</sup>yezi1616@163.com

**Keywords:** Al-4.5Cu alloy; rare earth Cerium; volume shrinkage; microstructure; pouring slope

**Abstract.** The effects of adding rare earth Cerium on Al-4.5Cu alloy microstructure, solidification range and volume changes in the solidification process are researched. Experiments show that rare earth Cerium will bring remarkable effects on the alloy microstructure, solidification and solidification shrinkage interval. When the quantity of rare earth Cerium is about 4 wt%, the solid-liquid two phase of Al-4.5Cu alloy will range from 640°C to 600°C. The grains of the alloy are refined, round. The volume shrinkage is only 68.6% of that without adding rare earth Cerium.

### Introduction

With the rapid development of aerospace technology, the requirement of materials with higher strength and better fracture toughness, stress corrosion resistance and fatigue properties becomes more and more strongly [1]. Cast aluminum alloy are widely used in various industries because of its advantages such as low density, high specific strength, easy processing, economic and so on [2,3]. A large number of studies have shown that it can narrow solidification temperature range, increase the intensity and plasticity of hot brittle zone, and refine the grains by adding microelements in aluminum-copper alloy [4-7]. To some extent, it can improve the whole mechanical properties of cast aluminum alloy greatly. Thermal fatigue properties, mechanical behavior of the alloy during solidification and the grain boundary state is closely related to the solidification process of alloy [8-9].

Al-4.5Cu is the matrix of casting Al-Cu system alloy. In this article, in order to improve the quality of alloy castings, the effects of rare earth Ce on the Al-4.5Cu solidification range, solidification volume change and the cast microstructure have been researched by adding rare earth Ce in Al-4.5Cu alloy.

### Experimental Procedures

**Experimental Equipments.** (1) Melting pot: Experimental use of graphite crucible and the box-type resistance furnace, the model of box-type resistance furnace is SX2-4-10, and its parameters are as below: voltage 220V, power 10kw, maximum working temperature 1000°C, and the normal working temperature 950°C.

(2) Temperature control: The temperature controller is KSW-8D-13, its operating parameters are: error of 1%, with K series of 101-type thermocouple, measuring range of 0-1200°C.

(3) Temperature remelting furnace: A furnace tube is used in the experiment.

(4) Data collection: Using the Advantech data acquisition module, with K-type thermocouple, temperature range of 0-1100°C.

(5) Mechanical balance: with an accuracy of 0.1mg.

(6) Analysis gauges: with an accuracy of 0.1ml.

**Experiment.** Material: aluminum ingot (mass content of impurities less than 0.1%), copper ingot (mass content of impurities less than 0.1%), rare earth Ce (mass content of impurities less than 0.1%). Put aluminum ingot into the box-type resistance furnace for smelting (using graphite crucible), and add a certain amount of copper into graphite crucible to prepare Al-4.5Cu alloy. Then join the rare earth Ce to prepare three kinds of Al-4.5Cu alloy with Ce content (mass percentage) was 0%, 1%

and 4% respectively. Exclude the gas of the prepared alloy composition and refine them, about 10min later, pour it to the slope water-cooled copper mold for casting at 700°C respectively. Take the samples at the same location after air-cooled. Grind the samples with 600#, 1000# sandpaper, and then polish it on the polisher. Finally, observe its microstructure after corroding the metallographic specimens with 0.5% HF acid solution.

In order to test the effects of different rare earth Ce content on the Al-4.5Cu solidification range, pour the prepared three kinds of alloy composition into the stainless steel graphite mold, and put the stainless steel graphite mold into a tube furnace with a temperature of 680°C then cool it with furnace. Record the temperature change throughout the solidification process with data acquisition module and draw the solidification curve.

To analyze the effects of different rare earth Ce content on the volume shrinkage of Al-4.5Cu alloy solidification process, pour the prepared three kinds of alloy composition at 700°C into the mold with a cavity volume of 60ml, and then cool them with the air. Weigh their mass and measure their volume after the samples have been cooled to the room temperature.

## Results and Discussion

Fig.1 shows the Al-Cu binary phase diagram. There is  $L \rightarrow \alpha(\text{Al}) + \text{Al}_2\text{Cu}$  binary eutectic reaction in the Al-rich side of the phase diagram. The limit of solubility of Cu in  $\alpha(\text{Al})$  is 5.7%, but as the temperature drops, the solubility of Cu in  $\alpha(\text{Al})$  decreases. Al-Cu alloy is an alloy which can be strengthened by heat treatment. Al-Cu alloy has high mechanical properties in the quench aging state.

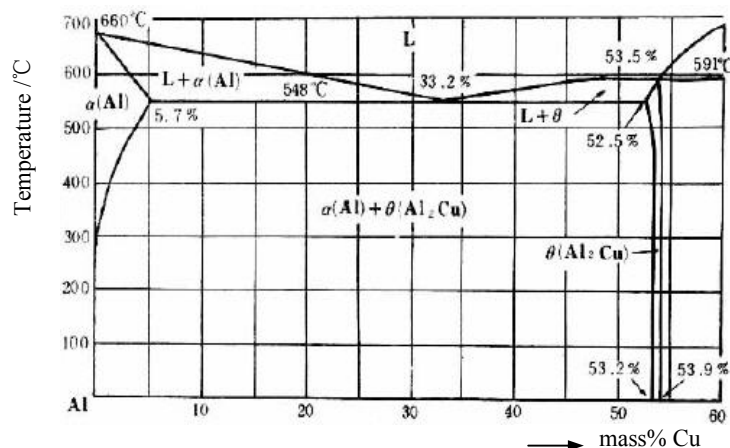


Fig.1 Al-Cu binary phase diagram

**Effects of Ce Content on Al-4.5Cu Alloy Solidification Range.** Fig.2 shows the solidification curves of Al-4.5Cu alloy when the adding amount of rare earth Ce was 0%, 1% and 4% respectively. When Ce addition is 0%, the alloy solidified from 650°C(beginning) to 540°C(ending), and the eutectic reaction occurred, then solidification nearly ended. When the rare earth Ce addition is 1%, the alloy started to solidify at 644°C, and finished solidification at 542°C. When the rare earth Ce addition is 4%, the alloy started to solidify at 639°C, and finished solidification at 600°C. By comparing the results above, Al-4.5Cu alloy solidification range can be changed by adding rare-earth Ce. The two-phase interval of the Al-4.5Cu alloy was 650°C-540°C when no Ce was appended and it will narrow when some Ce was increased. When the rare earth Ce addition amounted to 4%, an abrupt change occurred, the two-phase range was 639°C-600°C, and the whole solidification time was also significantly reduced. Al-Cu alloy is a kind of high-strength heat-resistant alloys early used, The application of Al-Cu alloy has been greatly hampered because of its wide crystal solidification range, alloy solidification process prone to hot cracking, porosity and segregation defects, etc. Adding Ce content of 4% makes Al-4.5Cu alloy solid-liquid temperature range is only 39°C, which

improve the casting properties of the alloy, and will broaden the scope of application of Al-4.5Cu alloys.

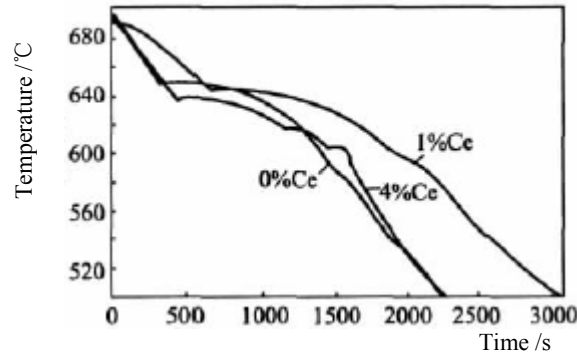


Fig.2 Solidification curve of Al-4.5Cu alloy

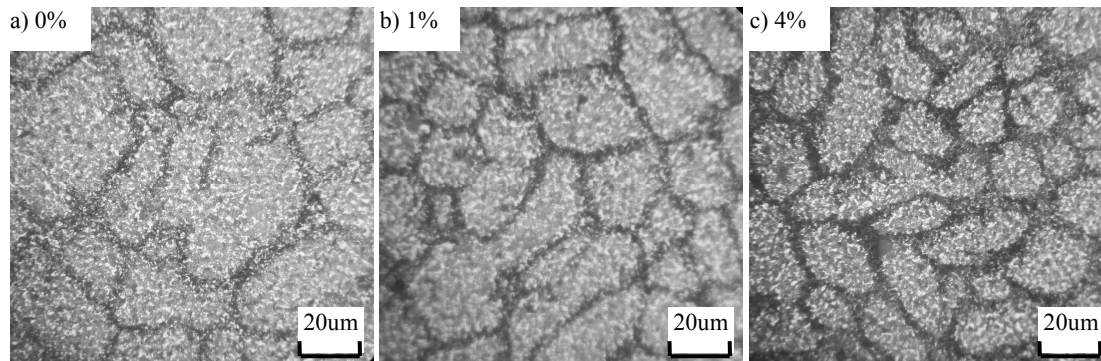


Fig.3 Microstructure of different content of Cerium

**Effects of Ce Content on Al-4.5Cu Alloy Casting Microstructure.** Fig.3 shows the metallographic microstructure of Al-4.5Cu alloy with the slope water-cooled copper mold casting at  $700^{\circ}\text{C}$  when Ce addition amount was 0%, 1% and 4% respectively. As can be seen from Fig.3, Fig.3 a) shows the microstructure of Al-4.5Cu alloy with no rare earth Ce addition, its grains was coarse, with well-developed dendrite, grain boundaries blurred. While its dendrite trend has been markedly inhibited when adding some rare earth Ce addition, with a larger number of primary  $\alpha$ -Al phase grains, and its grain was small, round, and distributed evenly. Comparing Fig.3(a),(b)and(c), the microstructure of Al-4.5Cu alloy became smaller and more round with the amount of Ce increased, while the content was around 4%, the alloy showed the best morphology. The addition of rare Earth Ce, made Al-4.5Cu alloy microstructure refine and round. It is conducive to strengthen the shrinkage process of the metal in the latter part of the process of alloy solidification, to increase the mobility of the alloy, and to improve the quality of the casting alloy, which can be used in a number of complex shape and special use requirements of the parts.

Table 1 Solidification parameters at different Ce addition

Alloy name	Cavity volume /ml	volume of sample /ml	Quality of sample /g
Al-4.5Cu	60	54.2	147.2
Al-4.5Cu-1Ce	60	55.3	150.5
Al-4.5Cu-4Ce	60	56.2	153.1

**Effects of Ce Content on Al-4.5Cu Alloy Solidification Shrinkage.** Table 1 shows the solidification parameters of Al-4.5Cu alloy pouring at  $700^{\circ}\text{C}$  with Ce addition amount of 0%, 1% and 4% respectively. In order to ensure the datum were accurate, stable and reliable enough, the datum in the table were the average values after 10 times' trial. It can be seen that the addition of

rare-earth Ce had significantly improved the volume shrinkage of Al-4.5Cu alloy in solidification process. With the addition amount of Ce increases, the volume shrinkage of the alloy decreases gradually. When the addition amount rises to 4%, the volume shrinkage is only 68.6% of that of no rare-earth Ce addition. This will help reduce the solidification shrinkage of Al-4.5Cu alloy in cast solidification processing, reduce the feeding, and increase the performance and quality of casting alloys.

### Conclusions

- (1) It will narrow the solid-liquid two-phase range to 639°C-600°C by adding rare-earth Ce about 4 mass% into Al-4.5Cu alloy.
- (2) It will refine the microstructure by adding rare-earth Ce into Al-4.5Cu alloy.
- (3) It will reduce the volume shrinkage of Al-4.5Cu alloy in solidification processing by adding rare-earth Ce into Al-4.5Cu alloy.

### Acknowledgements

This work was funded by Project GJJ08429, supported by the Foundation of Jiangxi Educational Committee of China. The authors would also like to express their appreciation to the Department of Mechanical Engineering of Tsinghua University and the Key Laboratory for Advanced Materials Processing Technology of Ministry of Education.

### References

- [1] S.K. Xie, X.Q. Zheng and R.X. Yi: Key Engineering Materials, Vol. 419(2010), p.517.
- [2] Z.Y. Chen, Q. Shu and Y.Y. Chen: Materials Science and Technology, Vol. 15(2007), p.718.
- [3] T.Y. Wan and Y.Z. Zhang: Materials for Mechanical Engineering, Vol. 21(1997), p.24.
- [4] R.X. Yi, S.K. Xie, W.X. Huang and Z.Q. Zheng: Hot Working Technology, Vol. 37(2008), p.30.
- [5] L. Sun, Q.C. Zhang and S.P. Yan: Acta Physica Sinica, Vol. 56(2007), p.3411.
- [6] R.X. Yi, S.K. Xie and X.L. Pan: Ordnance Material Science and Engineering, Vol. 32(2009), p.21.
- [7] R.X. Yi, S.K. Xie and X.L. Pan: Hot Working Technology, Vol. 38(2009), p.25.
- [8] N.C. Si, Q. Wu and G.Q. Li: Foundry, Vol. 55(2006), p.731.
- [9] Q.F. Li, L.B. Wang and B.Y. Yu: Foundry, Vol. 55(2006), p.1271.

## Simulation and Experimental Investigations of Fiber Diameter of Spunbonding Nonwovens by Means of the Air Jet Flow Field Model

B. Zhao<sup>1, a</sup>

<sup>1</sup>College of Textiles, Zhongyuan University of Technology, Henan, Zhengzhou 450007, China

<sup>a</sup>zhaobohenan@sina.com

**Keywords:** spunbonding, air jet flow field, polymer, fiber diameter, numerical computation.

**Abstract.** The air jet flow field models of spunbonding process are founded. It is simulated by means of the finite difference method. The numerical simulation computation results of distributions of the air velocity match quite well with the experimental data. The air drawing model of polymer is solved with the help of the distributions of the air velocity measured by a particle image velocimetry. The predicted filament fiber diameter agrees with the experimental data well.

### Introduction

Spunbonding process is used commercially as a single-step technology for converting polymer resin into nonwoven web, which dates back to 1950's [1]. In spunbonding process, a molten stream of polymer is extruded from the screw extruder and rapidly attenuated into filament fiber using aerodynamic device with the aid of high-velocity cool air stream. The fiber diameter is strongly affected by the air drawing model and the model of the air jet flow field. Earlier researchers have been studying the air drawing models of polymer spunbonding process, especially Spruiell J. E. and coworkers [1-4]. However, the reported air drawing model was quite elementary, all these models mentioned above were not based on using analytical and numerical methods. Moreover, there is not any literature regarding the study of the air drawing model of polymer and the model of the air jet flow field, which strongly affects the fiber diameter and web performance of spunbonding nonwoven. In this paper, we established the air drawing model of polymer in spunbonding process which based on numerical simulation computation results of the air jet flow field, and we adopt the finite difference method to simulate the air jet flow field. The fiber diameter can be predicted with the aid of air drawing model established. We also investigate the effects of process parameters such as the air initial temperature and the air initial velocity on fiber diameter and verify the model reliability of these relationships.

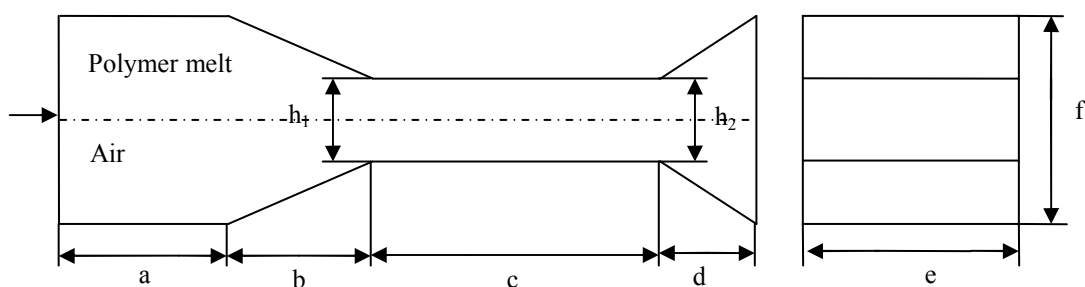


Fig.1 The flat narrow slot passage of drafting assembly in spunbonding process

### Numerical Simulation of the Air Flow Field Mathematical Model in Spunbonding Process

The flat narrow slot passage of drafting assembly shown in Fig.1 is used to yield nonwoven fabrics in a spunbonding process where a molten stream of polymer is extruded from the screw extruder and rapidly attenuated into filament fiber using aerodynamic device with the aid of high-velocity cool air stream. Because the fiber diameter of spunbonding process is intensely affected by the air jet flow

field, in this paper, we established a model of air jet flow field to simulate the flow field and solved numerically via the finite difference method. The distributions of the centreline x-component of air velocity along the x-axis are demonstrated.

**The Air Flow Field Theoretical Model of Spunbonding Process.** The air flow field of spunbonding process is considered to be a steady and viscous flow. The flow field is assumed to be two-dimensional. As k-ε model is the most widely used turbulence model in engineering computations in the case of high reynolds numbers. The air flow field of model consists of a continuity equation, a momentum equation, an energy equation, a constitutive equation, and a crystallization kinetics equation, a turbulent kinetic energy equation and a turbulent dissipation rate equation [5]. In this paper, we adopted k-ε standard model for computation. Below are some of the details, values of the constants of standard k-ε model are  $C_{1\varepsilon}=1.44$ ,  $C_{2\varepsilon}=1.92$ ,  $C_u=0.09$ [6]. The turbulent prandtl numbers are as follows:  $\sigma_k=1.0$ ,  $\sigma_\varepsilon=1.3$ ,  $Pr_t=1.0$ ,  $\sigma_t=0.9$ [2], where  $\sigma_t$ ,  $\sigma_k$  and  $\sigma_\varepsilon$  are prandtl numbers of turbulence, turbulent kinetic energy and turbulent dissipation rate, respectively.

Continuity equation

$$\frac{\partial(\rho u)}{\partial x} + \frac{\partial(\rho v)}{\partial y} = 0 \quad (1)$$

Where  $\rho$  is air density,  $u$  is the x-component of the air velocity,  $v$  is the y-component of the air velocity.

Momentum equation in z direction

$$\frac{\partial(\rho uu)}{\partial x} + \frac{\partial(\rho uv)}{\partial y} = 2 \frac{\partial}{\partial x} (\mu + \mu_t) \frac{\partial u}{\partial x} + \frac{\partial}{\partial y} (\mu + \mu_t) \left( \frac{\partial u}{\partial y} + \frac{\partial v}{\partial x} \right) - \frac{\partial p}{\partial x} + S_u \quad (2)$$

Here,  $\mu_t = \rho C_u \frac{k^2}{\varepsilon}$

Momentum equation in y direction

$$\frac{\partial(\rho vu)}{\partial x} + \frac{\partial(\rho vv)}{\partial y} = \frac{\partial}{\partial x} (\mu + \mu_t) \left( \frac{\partial u}{\partial y} + \frac{\partial v}{\partial x} \right) + 2 \frac{\partial}{\partial y} (\mu + \mu_t) \frac{\partial v}{\partial y} - \frac{\partial p}{\partial y} + S_v \quad (3)$$

Here,  $\mu = \nu \rho$ ,  $\mu_t = \nu_t \rho$

Where,  $P$  is the pressure of the air,  $\rho$  the density of the air,  $\nu_a$  the kinematic viscosity coefficient of the air,  $\nu_t$  the turbulent viscosity coefficient of the air,  $\mu$  the kinematic viscosity of the air,  $\mu_t$  the turbulent viscosity of the air.

Energy equation

$$\frac{\partial(\rho u T)}{\partial x} + \frac{\partial(\rho v T)}{\partial y} = \frac{\partial}{\partial x} \left[ \left( \mu + \frac{\mu_t}{\sigma_t} \right) \frac{\partial T}{\partial x} \right] + \frac{\partial}{\partial y} \left[ \left( \mu + \frac{\mu_t}{\sigma_t} \right) \frac{\partial T}{\partial y} \right] \quad (4)$$

Where,  $\sigma_t$  is the Prandtl number of turbulence.

Turbulent kinetic energy equation

$$\frac{\partial(\rho k u)}{\partial x} + \frac{\partial(\rho k v)}{\partial y} = \frac{\partial}{\partial x} \left[ \left( \mu + \frac{\mu_t}{\sigma_k} \right) \frac{\partial k}{\partial x} \right] + \frac{\partial}{\partial y} \left[ \left( \mu + \frac{\mu_t}{\sigma_k} \right) \frac{\partial k}{\partial y} \right] + G_k - \rho \varepsilon$$

$$\text{Here, } G_k = \frac{\mu_t}{\rho} \left[ 2 \left( \frac{\partial u}{\partial x} \right)^2 + 2 \left( \frac{\partial v}{\partial y} \right)^2 + \left( \frac{\partial u}{\partial y} + \frac{\partial v}{\partial x} \right)^2 \right] \quad (5)$$

Where,  $\sigma_\varepsilon$  is prandtl number of the dissipation rate of turbulent kinetic energy,  $\sigma_k$  is prandtl. Number of turbulent kinetic energy,  $\sigma_t$  is prandtl number of turbulence,  $\varepsilon$  the turbulent dissipation rate of air,  $k$  the turbulent kinetic energy of air.

Equation of dissipation rate of turbulent kinetic energy

$$\frac{\partial(\rho\varepsilon u)}{\partial x} + \frac{\partial(\rho\varepsilon v)}{\partial y} = \frac{\partial}{\partial x} \left[ \left( \mu + \frac{\mu_t}{\sigma_\varepsilon} \right) \frac{\partial \varepsilon}{\partial x} \right] + \frac{\partial}{\partial y} \left[ \left( \mu + \frac{\mu_t}{\sigma_\varepsilon} \right) \frac{\partial \varepsilon}{\partial y} \right] + \frac{C_{1\varepsilon} \varepsilon}{k} G_k - C_{2\varepsilon} \rho \frac{\varepsilon^2}{k} \quad (6)$$

Where  $\sigma_\varepsilon$  is prandtl number of dissipation rate of turbulent kinetic energy,  $C_u$ ,  $C_{\varepsilon 1}$  and  $C_{\varepsilon 2}$  are the constants of turbulent model, respectively.

**Boundary Conditions of the Air Flow Field Model.** As the flow field is symmetrical along the system centreline. So, the plane is chosen as the computation area, the following boundary conditions correlation is introduced.

(1)The conditions of upstream sections with the inlet are.

$$u = u_0, \quad v = v_0, \quad T = T_0, \quad k = \frac{3}{2} (u_{avg} I)^2, \quad \varepsilon = C_u^{\frac{3}{4}} \frac{k^{\frac{3}{2}}}{l}, \quad l = 0.07L \quad (7)$$

Where  $u_0$  is the x-component of the initial air velocity,  $v_0$  the y-component of the initial air velocity,  $T_0$  the initial air temperature,  $C_u=0.09$ ,  $u_{avg}$  is inlet average velocity,  $I$  is turbulent intensity of air,  $L$  is inlet characteristic dimension.

(2)The conditions of the wall sections are

$$u=0, \quad v=0, \quad T = T_w \quad (8)$$

(3)The centerline condition (x direction) are

$$\frac{\partial u}{\partial y} = 0, \quad \frac{\partial T}{\partial y} = 0, \quad v=0 \quad (9)$$

(4) The outer boundaries condition (y direction) is

$$\frac{\partial u}{\partial x} = \frac{\partial v}{\partial x} = \frac{\partial k}{\partial x} = \frac{\partial \varepsilon}{\partial x} = \frac{\partial T}{\partial x} = 0 \quad (10)$$

**Numerical Methods for Solving the Air Flow Field Model.** The air flow field model is solved numerically with the finite difference method. The preferred difference scheme for space independent variables is the second-order upwind difference scheme and the TDMA method is used to solve the difference equations. The SIMPLE algorithm is utilized to solve the problem of the velocity-pressure coupling. The staggered grid is adopted to avoid the tooth-like distributions of the velocity and pressure.

**Comparison of Theoretical Results with Experimental Data.** In order to testify the air flow field model, we measured and predicted the effects of spunbonding process parameters on fiber diameter. A particle image velocimetry (PIV-2100), produced by Denmark Dantec Inc. are utilized to measure the air velocity. In the application of PIV-2100, the air was seeded with oil soot (lampblack) aerosol particles in order for the laser light to be scattered and measured. Experiments are carried out on the flow field of spunbonding. The initial air velocity is 15m/s. The initial air temperature is kept unalterable in the measurements.

The distributions of the centreline x-component of air velocity along the x-axis are demonstrated in Fig.2. The experiment data are represented by dots, it was found that the theoretical (numerical) results obtained with the model match well with the experimental data.

### Effects of Spunbonding Processing Parameters on Filament Fiber Diameter

**The Relationship between the Initial Air temperature and Fiber Diameter.** Fig.2 shows the effect of the air initial temperature on fiber diameter which changing with the polymer melt temperature. The initial air temperature is 4.4, 15.6 and 26.8°C, in turn from top to bottom. As can be seen, the higher initial air temperature, the finer fiber diameter will be. This is primarily due to the fact that the initial air temperature increased firstly, the air drawing force increased and the degree of drawing increased which yield a finer fiber diameter. Secondly, when initial air temperature increased, the filament fiber cooled more slowly along the spinline, the drawing (tensile) time of polymer extended (lengthened) which result in a finer fiber diameter, Thirdly, when the initial air temperature increased, the viscosity and stress decreased which produce a finer fiber diameter.

**The Relationship between the Initial Air Velocity and Fiber Diameter.** Fig.3 gives the air initial velocity on fiber diameter which changing with the polymer melt temperature. The initial air velocity of 100, 150 and 250 m/s are considered. As the Fig. 4 shows, the higher initial air velocity are, the finer fiber diameters are. This is mainly attributed to the fact that the air initial velocity increased, the air drawing force increased and the degree of drawing increased which yield a finer fiber diameter.

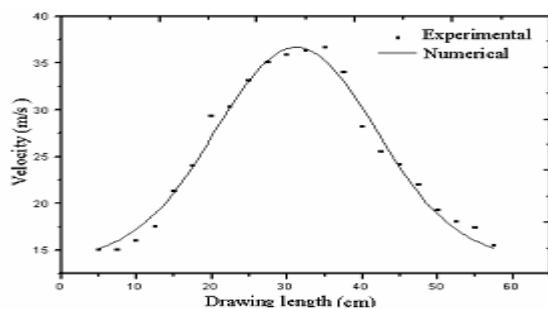


Fig.2 Distributions of centerline X-component of the air velocity along the x-axis

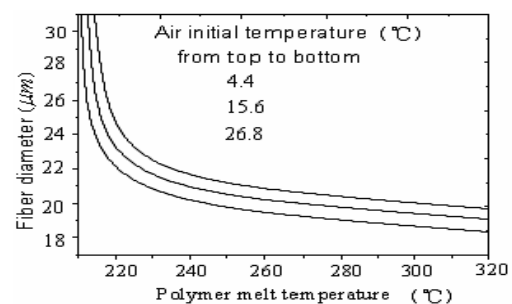


Fig.3 Effects of air initial temperature on the fiber diameter

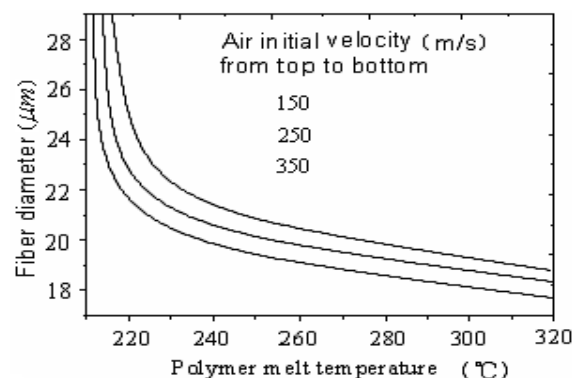


Fig.4 Effects of air initial velocity on the fiber diameter

### Conclusions

The air jet flow field models of polymer in spunbonding process are founded. We numerically simulated the air jet field model with the finite difference method. Computation results of the distributions of the x-components of air velocity along the spinline during spunbonding process are in accord with the experimental data well. The newly developed formulas are introduced into spunbonding air drawing model to predict the fiber diameter. The predicted results coincide well with

---

the actually measured data, which reveal that these models are accurate and also show this area of research has great potential in the field of computer assisted design in spunbonding nonwoven process and technology.

### Reference

- [1] N. Hajji: INDA J. Nonwovens Res. Vol. 4(1992) No. 2, p.16-21.
- [2] S. Misra: INDA J. Nonwovens Res. Vol. 5(1993) No. 3, p.13-19.
- [3] S. R. Malkan: Inter. Nonwovens J. Vol. 6(1994) No. 2, p. 24-50.
- [4] R. L Smorada: INDA J. Nonwovens Res. Vol. 3(1991) No.4, p.26-28.
- [5] T. Chen: *Study on the air drawing in melt blowing nonwoven process* (Ph. D. Dissertation of Donghua University, Shanghai 2003)
- [6] E. Gate: Computational fluid dynamics, Pearson Education Limited, 1996, p.45-76.

## Numerical Simulation of Accumulative Forming Bipolar Plates of Fuel Cell

XU Zhenying<sup>1, a</sup>, Wang Jingjing<sup>1, b</sup>, Ding Sheng<sup>1, c</sup>, WEN Wu<sup>1, d</sup>, WANG Yun<sup>1, e</sup>  
and YIN Bifeng<sup>1, f</sup>

<sup>1</sup>School of Mechanical Engineering, Jiangsu University, 301 Xuefu Road, Zhenjiang 212013, China  
<sup>a</sup>zhyxu77@163.com, <sup>b</sup>619wjj@163.com, <sup>c</sup>dsqph@163.com, <sup>d</sup>3040815016@163.com,  
<sup>e</sup>wangyun@ujs.edu.cn, <sup>f</sup>ybf@ujs.edu.cn

**Keywords:** Fuel cell; Bipolar plate; Accumulative forming; Numerical simulation

**Abstract.** The bipolar plate is the key part in the fuel cell. It is difficult to produce the micro flow channel of bipolar plates with high accuracy. In order to solve this problem, we present one new forming techniques, accumulative forming, for the fabrication of micro flow channels. With the utilization of the software ABAQUS, finite element model of the bipolar plate with the 20mm×20mm×0.2mm is developed to simulate the accumulative forming and obtain the forming rules. The simulation results are about the plate's thickness change and deformation. It shows that the thickness reduction decreases gradually from the center of the channel to the outside with the maximal magnitude in the starting point of accumulative forming. The maximum thinning ratio is 15.85%, which is in the forming limit scope. The simulation demonstrates the feasibility of the accumulative forming and good formability.

### Introduction

Fuel cells will be the fourth-generation electric power equipment and the alternative of combustion engine as it has the advantages over the water power, firepower and nuclear energy. The fuel cell is composed of anode, cathode and ionic conductive electrolyte, which is an energy-transforming device that directly transforms chemical energy of hydrogen or hydrogenous fuel and oxidant into electric energy. With the sustainable fuel feed, the current supply of fuel cell will never stop. Besides, the final reactant of fuel cell is pollution-free water or small amount of carbon dioxide<sup>[1]</sup>.

PEMFC (Proton exchange membrane fuel cells) is one kind of fuel cells that takes solid proton exchange membrane as electrolyte. PEMFC has some characteristics including quick start at low temperature, zero emissions, so it is considered as the best power candidate for electric car, submarine and some portable power supply<sup>[2]</sup>. The bipolar plate, which influences not only the cell stack performance but also the stack cost, is a vital component of PEMFC. Bipolar plates has the functions of isolating and uniformly allocating reacting gas, collecting the current, mechanical support, hydro-thermal management, connecting single battery. As metal material has high mechanical strength, better electrical and temperature conductivity, it can reduce thickness of bipolar plate significantly with the result of specific power increase of PEMFC. Therefore, the design and process of bipolar plates play an important pole in the performance, efficiency, and the cost of PEMFC. When the size of the flow field of bipolar plates is minimized to micrometer scale, the scale effects occur inevitably. Therefore, it is very important to develop the mass production technology of metal bipolar plate at low cost. This paper presents a new forming techniques, accumulative forming, for the fabrication of the bipolar plate. Numerical simulation is carried out to verify the feasibility of accumulative forming.

### Accumulative Sheet Forming Process

**Mechanism of Accumulative Forming.** Accumulative forming system shown in Fig.1 comprises the precision CNC (Computer Numerical Control) device 1, forming tool 2, blank holder 3, supporter 6

and sheet 7. First, the sheet metal with the appropriate dimensions is positioned on the supporter 6 and fixed by the blank holder 3. The diameter of forming tool 2 is the same as the flow channel's span, and its stroke of forming tool is the depth of flow channel. Forming tool goes down to reach the channel depth, then the tool travels according to the pathway of flow channels under the control of NC program. In this way, the whole flow channels of the bipolar plates for gas reaction can be obtained.

The accumulative forming is one method for shape the sheet through accumulative plastic deformation forming with the control of the tool movement. In accumulative forming process, the influencing factors are complicated. The current finite element simulation has become an effective tool to evaluate the performance of sheet metal forming process and the mould design. The accumulative forming is simulated by finite element software ABAQUS to obtain the forming rules and demonstrate its validity.

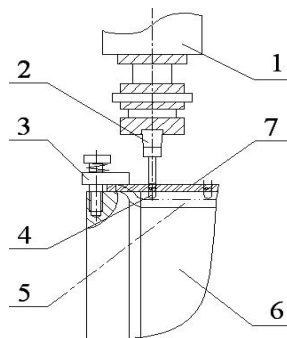


Fig.1 The schematic diagram of accumulative forming system

### Accumulative Forming Model for Finite Element Analysis

**Finite Element Model.** ABAQUS is the finite element codes developed by the HKS Inc, which is widely used in different domain. The material of the bipolar plate is copper H62, the size is 40mm×40mm×0.2mm. The actual size of forming region is 20mm×20mm because of the blank holder occupy. The material of forming tool, which is treated as rigid body, is 40Cr. The material parameters are shown in Table 1.

Table 1 Material parameters

	Forming tool	Bipolar plate
Material	40Cr	Copper H62(Y2)
Density /kg.m-3	7820	8920
Elastic modulus/MPa	211000	1.19E+11
Poisson's ratio	0.30	0.33

According to the finite element model of accumulative forming, four-node explicit shell element is selected for analysis. The model is composed of forming tool, blank holder, plate and die, as shown in Fig.2. Through imposing the fixed boundary conditions by the cavity die and blank holder, we can achieve the compression on the sheet. So it is easy to form without affecting the plate's material flow in the axial.

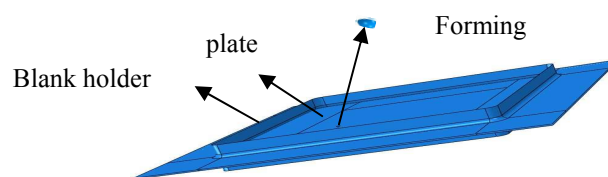


Fig.2 Finite element model of bipolar plates in accumulative forming

In the forming process, the force applied on the plate is passed through the contact between the metal sheet and the forming tool. Because contact type between the sheet and the forming tool is the

point contact, the accumulative forming process is more complex than the traditional one and the convergence impact of the calculation is greater. The choice of the contact type is very important. According to moving characteristics of the forming tool, we choose face-face contact type. In the contact analysis, due to the complexity of the problem, it is hard to determine the direction of the contact. We choose the automatic contact type, in which the target surface and the contact surface are arbitrarily<sup>[3]</sup>.

**The Sets of Punch Movement Path.** Straight channel structure is more common, while the serpentine multi-channel has a lot of flexibility that can change the number and length of flow channels according to different needs with no change in the area and shape of the flow plate [4].

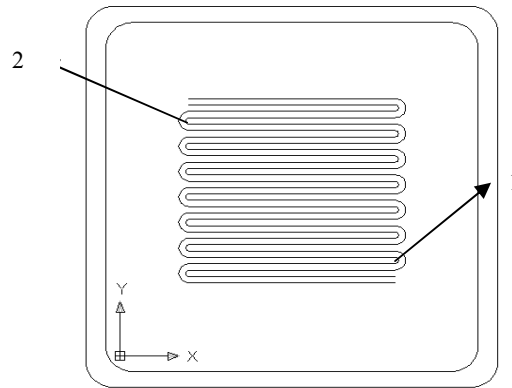


Fig. 3 Serpentine flow field of single-channel

As the simulation is performed to verify the feasibility of accumulative forming, the FE model of the serpentine single-channel is developed to reduce the time and cost of the calculation. According to the flow field structure of the bipolar plate, we use the NC program to control the pathway of the forming tool that is in accordance with the centerline of flow channels. As shown in Fig.3, the forming tool moves in the preset path from starting point 1 to the terminal point 2 in one-time to complete the forming process of flow channels of the bipolar plate.

### The Analysis Result and Discussion

Contours of the section thickness (STH) of the bipolar plate from FEM simulation are shown in Fig. 4. The following observations can be made from Fig. 4.

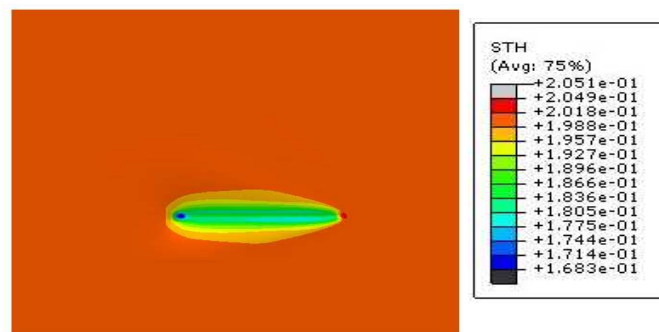


Fig. 4 Section thickness of the bipolar plate in accumulative forming

The STH contours are in the form of oval. The thickness thinning along the centerline of the channel is greater than the outside, and thinning decrease gradually from the channel centerline to the outside. About one tenth of the distance away from channel centerline, no thinning occurs. Actually, this phenomenon is in accordance with Saint-Venant principle.

The maximum thickness thinning appears in the starting point of accumulative forming. The thickness changes uniformly in the remaining regions of the plate. In fact, during the accumulative forming, the forming tool will stay in the starting point for seconds to maintain pressure before moving to the next step. However, the forming is performed continuously without pressure maintaining between two steps in actual simulation, so the thickness thinning reaches the maximum in the starting point of flow channel.

According to the failure criteria, the thinning ratio is controlled under the 25%-30% to avoid the failure in the sheet metal forming. According to the Fig.4, we can find that the largest thickness reduction is 0.03175 mm and the largest thinning rate is 15.85%. So this accumulative forming method is feasible for bipolar plate fabrication.

### Summary

One new forming technique for bipolar plate, accumulative forming, is initialized. In this new approach, forming tool with the same profile as the flow channel of the bipolar plate goes straight in the stroke to reach the channel depth, then the tool travels according to the pathway of flow channels under the control of NC program to form the whole channels. FEM is an effective method to evaluate the performance and formability of process. Therefore, finite element model of the plate with the size 20mm×20mm×0.2mm is developed and simulated. The simulation results of the section thickness show, that thickness reduction decreases gradually from the center of the channel to the outside with the maximal magnitude in the starting point of accumulative forming. The maximum thinning ratio is 15.85%, ensuring the good formability. It also demonstrates the feasibility of the accumulative forming.

### Acknowledgment

Thanks for supports from the National Natural Science Foundation of China (50805069), Postdoctoral Foundation of China (20090451174) and the Postdoctor Foundation of Jiangsu Province (0802024C).

### References

- [1] W.P. Li, X.X. Guo: submitted to Chinese Oil Companies (2005).
- [2] Y. Li, L.S. Wang: *Fuel cell* (Metallurgy Industry Press, Beijing 2000).
- [3] S. Jiang, J.Z. Gao and L.L. Jia: Chinese Manufacturing Information Vol. 38 (2009), p17-20.
- [4] Wilson M S, et al. U.S. Patent 5, 641, 586. (1997).

## Low Temperature Synthesis and Luminescent Properties of $\text{Ca}_2\text{SnO}_4: \text{Eu}^{3+}$

LI Yuzhong<sup>1, a</sup>, Zhou Xiaochun<sup>2, b</sup>

<sup>1</sup>Key Laboratory of Numerical Control Technology of Guangdong Higher Education Institutes,  
Mechanical and Electronic Department of Guangdong Polytechnic Normal University; Guangzhou  
510635, China

<sup>2</sup>School of Chemistry and Chemical Engineering, Jinggangshan University, Ji'an 343009, Jiangxi,  
China

<sup>a</sup>liyuzh@gdin.edu.cn, <sup>b</sup>ncdxzxc@163.com

**Keywords:**  $\text{Ca}_2\text{SnO}_4: \text{Eu}^{3+}$ ; Luminescence; Low temperature solid state reaction; Intensity ratio.

**Abstract.** A novel red emitting phosphor,  $\text{Ca}_2\text{SnO}_4: \text{Eu}^{3+}$ , was prepared by the low temperature solid state reaction. X-ray powder diffraction (XRD) analysis confirmed the formation of  $\text{Ca}_2\text{SnO}_4: \text{Eu}^{3+}$ . Scanning electron-microscopy (SEM) observation indicated a narrow size distribution of about 500 nm for the particles with spherical shape. Under 396 nm excitation, the  $\text{Ca}_2\text{SnO}_4: \text{Eu}^{3+}$  phosphor exhibits novel red emission at about 613 nm which is assigned to the  $5D_0 \rightarrow 7F_2$  electric-dipole transition. Furthermore, the emission transition  $5D_0 \rightarrow 7F_2$  has been found to be more prominent over the normal orange emission transition  $5D_0 \rightarrow 7F_1$ .

### Introduction

The efficiency of phosphor has been advanced by both a new host material and improved synthetic technique [1]. The luminescent properties of phosphors are strongly dependent on the crystal structure of host materials. The luminescence behaviors of the  $\text{Eu}^{3+}$  activator have been extensively studied by many researchers [2,3,4]. According to the reports, the emission of  $\text{Eu}^{3+}$  activator depends on the crystal environment. The  $5D_0 \rightarrow 7F_1$  transition  $\text{Eu}^{3+}$  ion gives an orange emission by forming a centro-symmetrical environment for  $\text{Eu}^{3+}$  ions, while the  $5D_0 \rightarrow 7F_2$  transition  $\text{Eu}^{3+}$  ion exhibits a red emission by forming a non centro-symmetrical environment for  $\text{Eu}^{3+}$  ions.

Calcium stannate ( $\text{Ca}_2\text{SnO}_4$ ) has been a good candidate for a wide range of applications. The host material of novel emitting phosphor,  $\text{Ca}_2\text{SnO}_4$  has been studied by some researchers [5, 6].

However, there is still relatively limited amount of research available on the sintering behavior of Ca - Sn - O system, especially, according to the reports, the product  $\text{Ca}_2\text{SnO}_4$  was formed above  $1200^\circ \text{C}$ . In the present work it was attempted to prepare  $\text{Ca}_2\text{SnO}_4: \text{Eu}^{3+}$  phosphors by the low temperature solid state reaction and investigate their luminescent properties under UV excitation.

### Experimental

A.R. grade of Sn,  $\text{Ca}(\text{NO}_3)_2 \cdot 4\text{H}_2\text{O}$ , and  $\text{HNO}_3$ .  $\text{Eu}_2\text{O}_3$  (99.99 %) was purchased from Shanghai Yuelong New Materials Corporation.  $\text{Eu}(\text{NO}_3)_3$  was prepared by dissolving 0.2 mmol  $\text{Eu}_2\text{O}_3$  in nitric acid (63- 65%) and then evaporating the solvent in crucible. A two - step method was employed for the  $\text{Ca}_2\text{SnO}_4: \text{Eu}^{3+}$  powders preparation including the synthesis of  $\text{H}_2\text{SnO}_3$  and then converts it into  $\text{Ca}_2\text{SnO}_4$  by calcination to obtain  $\text{Ca}_2\text{SnO}_4: \text{Eu}^{3+}$  powders.

In a typical synthesis of  $\text{H}_2\text{SnO}_3$ , Sn was prepared by dissolving in nitric acid (63-65%) and then evaporating the solvent in crucible, in the crucible experiments have repeatedly done to ensure the complete reaction of Sn. the reaction equation as follows:



A typical experimental procedure for the synthesis of  $\text{Ca}_2\text{SnO}_4: \text{Eu}^{3+}$  powders are as follows. In the as-prepared  $\text{Eu}(\text{NO}_3)_3$  crucible, 0.005 mol the as-prepared  $\text{H}_2\text{SnO}_3$  was fed with 0.01 mol of  $\text{Ca}(\text{NO}_3)_2 \cdot 4\text{H}_2\text{O}$ , the mixture was continually ground at room temperature, After 10 min of grinding, 4 ml deionized water was added to the above mixture. Under continuous stirring and heating at about  $80^\circ\text{C}$ , as water evaporated, the solution became viscous and finally formed a gel. Subsequently, the gel was dried at  $100^\circ\text{C}$  for 4 h to yield a xerogel. The obtained xerogel was placed into a furnace preheated to a definite temperature ( $740^\circ\text{C}$ ) and calcined for 40 min.

X-ray diffraction (XRD) patterns were measured using a BRUKERD8 FOCUS with  $\text{Cu K}\alpha$  radiation ( $\lambda=0.15418\text{ nm}$ ), at a scanning rate of  $4.0^\circ\cdot\text{min}^{-1}$ . PL emission/excitation spectra were measured using an F-4500 fluorescence spectrometer (Hitachi). The sizes and morphologies of the as-synthesized samples were studied by KYKY2AMARY21000B scanning electron microscope (SEM). Fourier transform infrared spectroscopy (FTIR, AVATAR370) were used to measure phosphors powder with the KBr pellet technique. All the measurements were carried out at room temperature.

## Results and Discussion

XRD was used to examine the crystal structure and phase purity of the products and the typical XRD patterns of the 0.01 mol of  $\text{Ca}(\text{NO}_3)_2 \cdot 4\text{H}_2\text{O}$  co-doped synthesized  $\text{Ca}_2\text{SnO}_4: \text{Eu}^{3+}$  samples are shown in Fig.1. All mainly reflections in the patterns corresponding to orthorhombic crystal system structure  $\text{Ca}_2\text{SnO}_4$ , and this observation indicates that the mainly phase of  $\text{Ca}_2\text{SnO}_4$  was completed by the low temperature (at  $740^\circ\text{C}$ ) solid state reaction, this may be ascribed to the synthesis of  $\text{H}_2\text{SnO}_3$  and effects of low temperature solid-state reaction.

Fig. 2 shows the FTIR spectra of co-doped synthesized  $\text{Ca}_2\text{SnO}_4: \text{Eu}^{3+}$  samples. The absorption at  $3430\text{ cm}^{-1}$  indicates the presence of hydroxyl-groups, which is probably due to the fact that the spectra were not recorded in situ and some water readsorption from the ambient atmosphere has occurred. The IR spectrum of the sample had distinct absorption peaks at 660, and  $880\text{ cm}^{-1}$  relating to  $\text{Ca}_2\text{SnO}_4$ , this implied that the crystalline  $\text{Ca}_2\text{SnO}_4$  was obtained at  $740^\circ\text{C}$  low temperature.

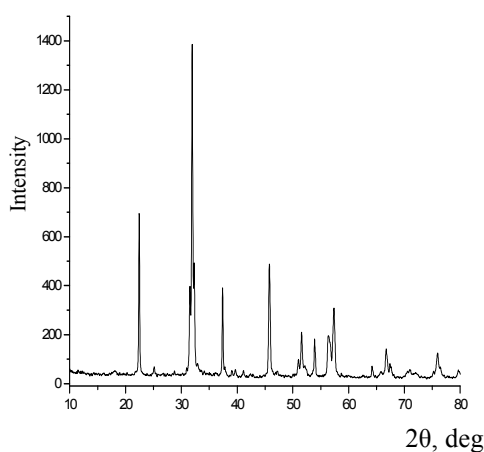


**Fig. 1.** XRD patterns of the as-prepared  $\text{Ca}_2\text{SnO}_4: \text{Eu}^{3+}$

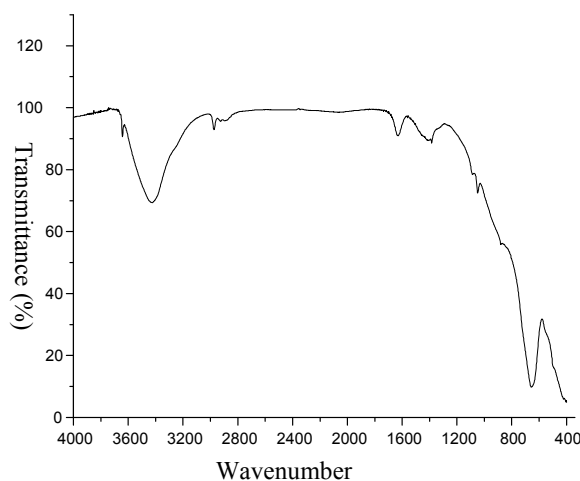
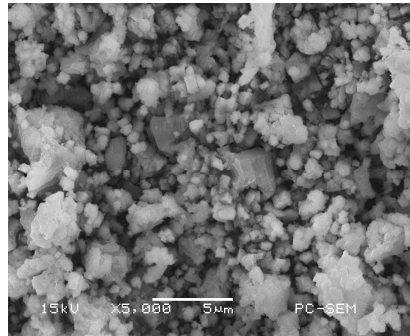


**Fig. 2.** FTIR spectra of the as-prepared  $\text{Ca}_2\text{SnO}_4: \text{Eu}^{3+}$

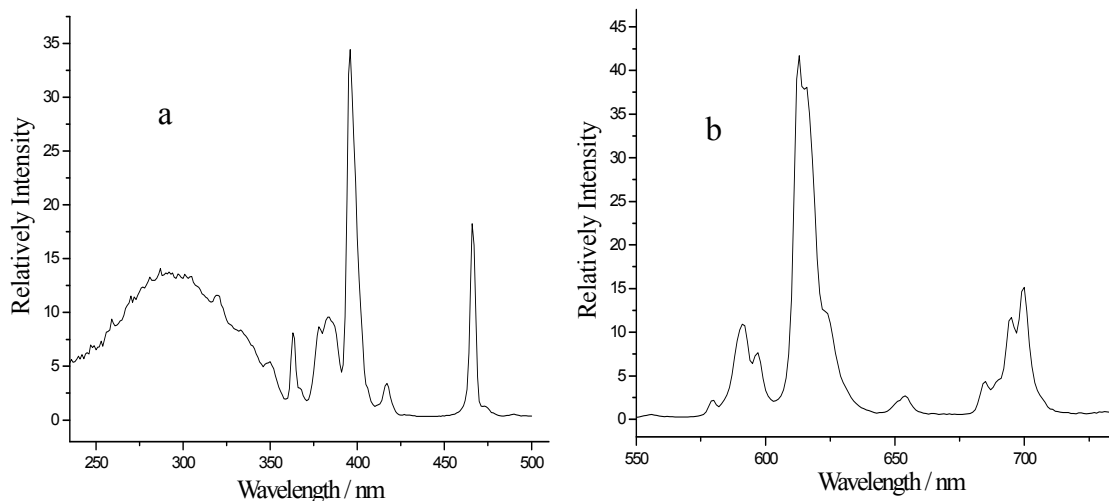
The morphologies of as-obtained co-doped synthesized  $\text{Ca}_2\text{SnO}_4: \text{Eu}^{3+}$  samples are examined with scanning electron microscopic (SEM). Fig.3 shows a typical SEM image of products obtained codopes. It is obvious that the 0.01 mol of  $\text{Ca}(\text{NO}_3)_2 \cdot 4\text{H}_2\text{O}$  co-doped synthesized  $\text{Ca}_2\text{SnO}_4: \text{Eu}^{3+}$  exhibits spherical-like morphology and the particle size is distributed uniformly in  $1\ \mu\text{m}$ .

Fig.4 presents excitation and emission spectra of  $\text{Ca}_2\text{SnO}_4: \text{Eu}^{3+}$  samples. From Fig. 4a, the excitation spectra of  $\text{Ca}_2\text{SnO}_4: \text{Eu}^{3+}$  under 613 nm emission. The excitation spectra show broad  $\text{Eu}^{3+} - \text{O}_2^-$  charge transfer (CT) absorption bands in the range of 232.6 - 358.4 nm, the peak of CT is

at 287.0 nm. The sharp lines in the spectra range from 300 to 500 nm correspond to direct excitation of the  $\text{Eu}^{3+}$  ground state to higher levels of the 4f-manifold, wavelength range 300- 500 nm, including  $7F_0 \rightarrow 5D_4$  (363 nm),  $7F_0 \rightarrow 5L_7$  (378, and 383 nm),  $7F_0 \rightarrow 5L_6$  (396 nm),  $7F_0 \rightarrow 5D_3$  (417 nm),  $7F_0 \rightarrow 5D_2$  (466 nm), the most intense transition excitation line located at 396 nm ( $7F_0 \rightarrow 5L_6$ ). Thus, emission spectra are presented upon the excitation at 396 nm. As is shown in Fig. 4b, the emission spectra of  $\text{Ca}_2\text{SnO}_4: \text{Eu}^{3+}$  under 396 nm excitation consist of several bands, the following emission transitions have been observed:  $5D_0 \rightarrow 7F_1$  (580, 591 and 597 nm),  $5D_0 \rightarrow 7F_2$  (613 nm),  $5D_0 \rightarrow 7F_3$  (654 nm), and  $5D_0 \rightarrow 7F_4$  (695, and 700 nm). The transitions are found to be split into components depending upon the host matrix. The phosphors exhibit red color under UV-source due to the most intense emission transition  $5D_0 \rightarrow 7F_2$  (electric dipole line), which indicates a non center-symmetrical environment for  $\text{Eu}^{3+}$  ions. The larger  $5D_0 \rightarrow 7F_2 / 5D_0 \rightarrow 7F_1$  intensity ratio indicates that the point symmetry of  $\text{Eu}^{3+}$  site is closer to an inversion center, and at the same time, the plausible explanation to the much larger  $5D_0 \rightarrow 7F_2 / 5D_0 \rightarrow 7F_1$  intensity ratio is that  $\text{Ca}_2\text{SnO}_4$  has an orthorhombic crystal system structure with low symmetry, when  $\text{Eu}^{3+}$  ions are doped in the  $\text{Ca}_2\text{SnO}_4$  host, according to regulations of radius,  $\text{Eu}^{3+}$  (0.101 nm),  $\text{Ca}^{2+}$  (0.099 nm),  $\text{Sn}^{4+}$  (0.071 nm),  $\text{Eu}^{3+}$  could occupy  $\text{Ca}^{2+}$  sites, thus, the excellent red emission transition  $5D_0 \rightarrow 7F_2$  has been found to be more prominent for  $\text{Eu}^{3+}$  ions



**Fig.3** SEM images of the as-prepared  $\text{Ca}_2\text{SnO}_4 : \text{Eu}^{3+}$



**Fig. 4.** spectrum of the as-prepared  $\text{Ca}_2\text{SnO}_4: \text{Eu}^{3+}$ :  
(a) excitation (em = 615 nm); (b) emission (ex = 395 nm)

## Conclusions

In summary, a novel red phosphor  $\text{Ca}_2\text{SnO}_4: \text{Eu}^{3+}$  has been synthesized by low temperature solid state reaction. The mainly phase of  $\text{Ca}_2\text{SnO}_4: \text{Eu}^{3+}$  phosphor is formed by sintering at 740 °C, the SEM results indicates morphology is regular. Two dominant bands of  $\text{Eu}^{3+}$  ions, which corresponding to

transitions of  $5D_0 \rightarrow 7F_1$  (orange),  $5D_0 \rightarrow 7F_2$  (red), transition  $5D_0 \rightarrow 7F_2$  (electric dipole line), were prominent in the emission spectra indicating a non - centro symmetrical environment for  $\text{Eu}^{3+}$  ions. In summary, a novel red phosphor  $\text{Mg}_2\text{SnO}_4:\text{Eu}$  has been synthesized by low temperature solid state reaction. The mainly phase of  $\text{Mg}_2\text{SnO}_4:\text{Eu}$  phosphor is formed by firing at  $740^\circ\text{C}$ , the SEM results indicates morphology is regular. Two dominant bands of  $\text{Eu}^{3+}$  ions, which corresponding to transitions of  $5D_0 \rightarrow 7F_1$  (orange),  $5D_0 \rightarrow 7F_2$  (red), transition  $5D_0 \rightarrow 7F_2$  (electric dipole line), were prominent in the emission spectra indicating a non centro – symmetrical environment for  $\text{Eu}^{3+}$  ions.

## References

- [1] H. K. Jung, D. S. Park and Y. C. Park: Materials Research Bulletin Vol.34(1999) No.1, p.43-51.
- [2] H. Lai, A. Bao and Y.M. Yang, *et al*: Journal of Nanoparticle Research (2008) No. 10, p. 1355 - 1360.
- [3] E. A. Morais, L. V. A. Scalvi and A. Tabata, *et al*: Journal of Materials Science (2008) No. 43, p. 345-349.
- [4] H.L. Zhu, H. Yang and D.L Jin, *et al*: Journal of Nanoparticle Research (2008) No. 10, p. 1149 - 1154.
- [5] A. A. Al Shahrani: Journal of Materials Science: Materials in Electronics (2005)No.16, p. 193 - 196.
- [6] Y.C. Chen, Y.W. Chang, and B. Tsai: Optical Materials Vol.27(2005) No. 12, p. 1847-1878

## **Study on Load-velocity Dynamic Property of Piston-type Hydraulic Cylinder based on SIMULINK**

JIN Xiangshu<sup>1, a</sup>, DING Shiyan<sup>1, b</sup>, TANG Xuezhong<sup>2</sup> and HU Zhixi<sup>2</sup>

<sup>1</sup>School of Mechanical and Electronical Engineering, Changzhou Institute of Technology, Changzhou, Jiangsu 213002, China

<sup>2</sup>School of Information Technology, Changzhou Institute of Technology, Changzhou, Jiangsu, 213002 China

<sup>a</sup>zhongshanfyking@126.com, <sup>b</sup>jinxs@czu.cn

**Keywords:** SIMULINK; Hydraulic cylinder; Dynamic property; Modeling; Simulation

**Abstract.** According to liquid continuity theory and the dynamic equilibrium conditions, established a piston-type hydraulic cylinder mathematical model. Founded the simulation model in the SIMULINK/ MATLAB environment and solved its unit-step response based on the relation between load and velocity, gave the hydraulic cylinder design parameter and the medium character's influence to its unit-step response, summarized the intrinsic relations between parameters and the time domain index, provided the theory basis to optimize the hydraulic cylinder dynamic property. The hydraulic cylinder load - speed dynamic performance studies have shown that this method does not require complicated programming, simulation models can be visually established, and can greatly shorten the design cycle, reduce design costs, and improve product performance.

### **Introduction**

Modern hydraulic driving system is developing toward complexity, heavy-load, light-weight and high-speed. The dynamic behavior of hydraulic control system is gradually taken seriously and becomes one of the important indexes to evaluate a system's function. It is far from enough for a designer who designs modern hydraulic system, if he only knows the system can drive load from one state to another and its static behavior. he must know the load's movement, the system's parameters' (such as pressure, speed, displacement) variation principle through time and the system's characters such as the stability of the system reaction, rapidity, accuracy, hydraulic shock, noise, and so on.

The dynamic simulation of hydraulic system is of great importance to the analysis of the hydraulic system dynamic behavior, the improvement of the hydraulic design and reliability of a hydraulic system. MATLAB is a kind of high-level software that is a set of scientific computing, automatic control, signal processing and other functions with great efficiency. Meanwhile MATLAB provides a software package called SIMULINK, it can be easily used to the modeling, simulation and analysis of a dynamic system, it provides a new method to conduct the simulation research of a hydraulic circuit and can improve the efficiency of the design of a hydraulic system greatly.

This paper takes piston hydraulic cylinder as an example, analyzes and establishes its mathematical model. This research establishes a simulation model based on SIMULINK/ MATLAB and gives a solution, so to find out the relations between system parameters and the dynamic behavior.

### **Establishment of Mathematical Model of Hydraulic Cylinder**

Consider a single-acting hydraulic cylinder as Figure 1,  $m$  is the mass (kg) of the piston and the moving parts,  $F$  is the load of the moving parts (N). The hydraulic oil will push the piston and the moving parts to move along the horizontal direction when it filled into the pressure chamber.

Continuity equation [1] can be obtained according to the theory of fluid:

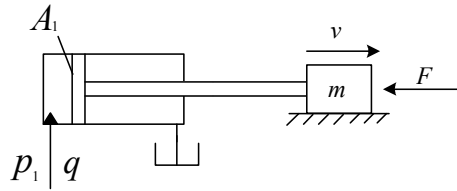


Fig. 1 Hydraulic cylinder working diagram

$$q = A_1 v + \lambda_c p_1 + \frac{V_h}{\beta} \frac{dp_1}{dt} \tag{1}$$

Where,  $p_1$  is the working chamber pressure of hydraulic cylinder, MPa;  $q$  is the flow into hydraulic cylinders, m<sup>3</sup>/min,  $A_1$  is hydraulic cylinder piston area, m<sup>2</sup>;  $\lambda_c$  is the leakage coefficient of hydraulic cylinder, m<sup>5</sup>/N·s;  $V_h$  is the volume of hydraulic cylinder high-pressure chamber and pipes, m<sup>3</sup>;  $\beta$  is the effective bulk modulus of oil, Pa.

Hydraulic cylinder piston dynamic balance equation is:

$$p_1 A_1 = m \frac{dv}{dt} + Bv + F \tag{2}$$

Where, B is the oil viscous damping coefficient, N/ (m/s).

The following expressions can be obtained according to LAPLACE transform on the formula (1) and (2).

$$\frac{mV_h}{\beta} S^2 + \left( \frac{V_h \cdot B}{\beta} + m\lambda_c \right) S + A_1^2 + B\lambda_c \quad V(S) = Q(S) - \frac{\lambda_c + \frac{V_h}{\beta} S}{A_1} F(S) \tag{3}$$

Equation (3) shows the mathematical model of Fig.1 which has transfer function form. According to this equation, the system block diagram [2] [3] when  $Q(S)=0$  can be obtained as shown Fig. 2.

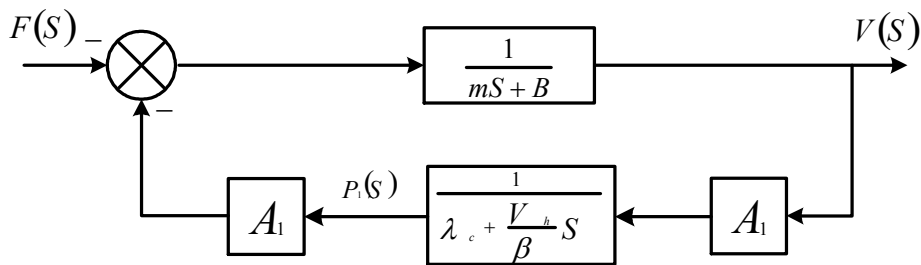


Fig. 2 System block diagram when  $Q(S)=0$

Obviously it is a second-order system, which consists of two main parameters, non-damped natural frequency:

$$\omega_n = \sqrt{\frac{(A_1^2 + B\lambda_c)\beta}{mV_h}} \text{ rad/s} \tag{4}$$

Damping ratio:

$$\xi = \frac{BV_h + m\lambda_c\beta}{mV_h} \times \frac{1}{2\sqrt{(A_1^2 + B\lambda_c)\beta/mV_h}} = \frac{\omega_n}{2} \times \frac{BV_h + m\lambda_c\beta}{(A_1^2 + B\lambda_c)\beta} \tag{5}$$

The following major factors which affect dynamic performance of hydraulic cylinder can be concluded according to equation (4) and (5).

**Hydraulic Cylinder Area  $A_1$ .** Larger the area, higher the system natural frequency but lower the system damping ratio.

**The Mass (Kg) of the Piston and the Moving Parts  $m$ .** Larger the mass, lower system natural frequency but higher the damping ratio.

**The Volume of Hydraulic Cylinder High-pressure Chamber and Pipes  $V_h$ .** Larger the volume, lower higher the system natural frequency but higher the system damping ratio.

**Leakage Coefficient of Hydraulic Cylinder  $\lambda_c$ .** The greater the coefficient is, the greater the system damping ratio is.

**Effective Bulk Modulus of Oil  $\beta$ .** The greater the coefficient is, the higher the damping ratio and the system natural frequency are.

**Solution and Establishment of Simulation Model in SIMULINK Environment [4-6]**

SIMULINK is highly integrated by MATLAB; it is a software package for dynamic system modeling, simulation and analysis. It not only supports continuous, discrete or a mixture of both linear and nonlinear systems, but also supports the system with a variety of sampling frequency. The main difference between SIMULINK and MATLAB is that its interaction with users is Windows-based graphical input, and users can put more energy into building system models rather than programming. In the SIMULINK environment, users can "paint" the system model only by mouse in the model window, and then simulate directly. SIMULINK contains many sub-model libraries such as SINKS (input mode), SOURCE (input source), LINEAR (linear part), NONLINEAR (non-linear part), CONNECTIONS (connect and interface) and EXTRA (other sectors), etc., and each sub - model library contains the corresponding functional blocks. Users can also customize and create their own modules.

Run MATLAB software, click the SIMULINK button, then create hydraulic cylinder system simulation model when  $Q(S) = 0$ . The simulation model according to preset simulation parameters in Table 1 is shown in Fig.3:

Table 1 Simulation parameters

$m$ [Kg]	$A_1$ [m <sup>2</sup> ]	$V_h$ [m <sup>3</sup> ]	$\lambda_c$	$\beta$ [N·m <sup>-2</sup> ]	B	F[N]
3000	2.125e-3	1.31e-3	1.5e-11	1.2e9	2100	500

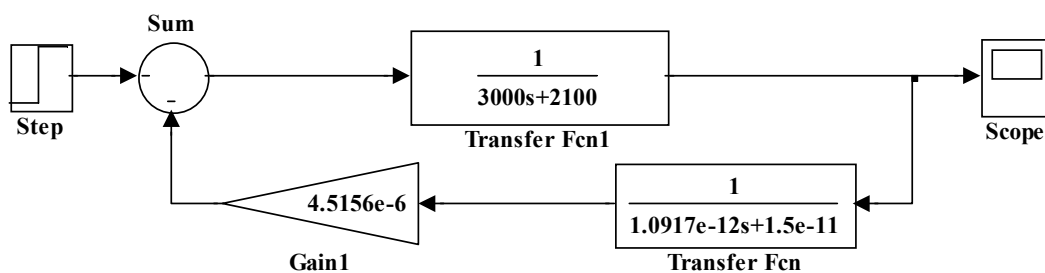


Fig.3 System Simulation Model When  $Q(S) = 0$

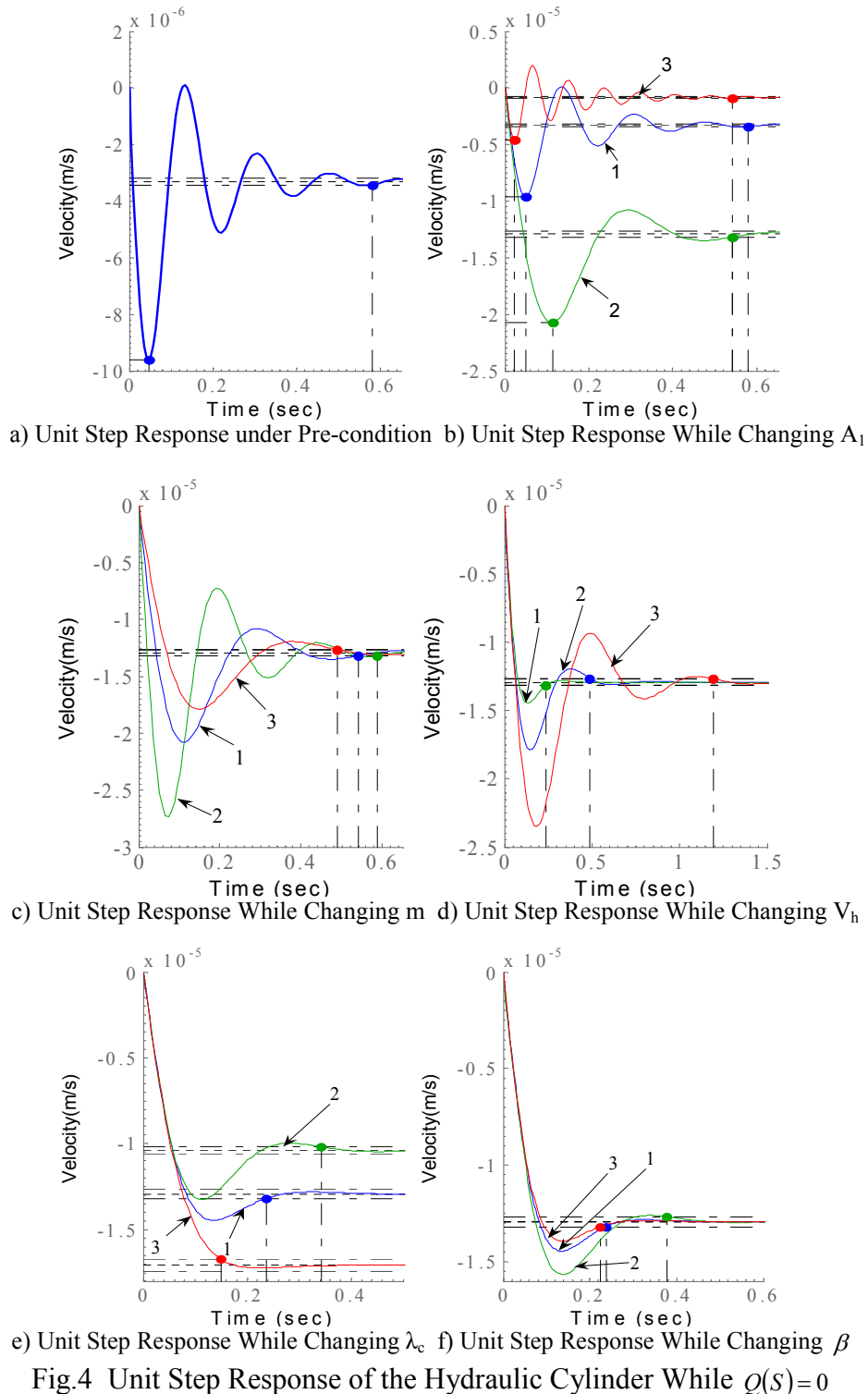
In Fig. 3, Transfer Fcn is from CONTINUOUS module, and it is the part transfer function with incorporated parameters. Step is the unit step input signal which comes from SOURCE module. Scope is a virtual oscilloscope which comes from SINKS module and can observe the system time response.

The system simulation results can be get as shown in Figure 4a) when select START option of Simulation in the SIMULINK software interface. When gradually change the system structure

parameters and fluid medium parameters such as  $A_1$ ,  $m$ ,  $V_h$ ,  $\lambda_c$ , and  $\beta$  as shown in Table 2, the corresponding system unit step response can be obtained as shown in Fig. 4b), c), d), e) and f):

Table 2 Hydraulic cylinder system parameter configuration table

Curve Number	Fig. a)	Fig. b)	Fig. c)	Fig. d)	Fig. e)	Fig. f)
	Initial Value	Change $A_1$	Change $m$	Change $V_h$	Change $\lambda_c$	Change $\beta$
1	Initial Value	2.1250e-3	3000	1.310e-3	1.5e-11	1.2e9
2	Initial Value	1.0625e-3	1500	0.655e-3	1.2e-11	0.9e9
3	Initial Value	4.2500e-3	4500	2.620e-4	2.0e-11	1.4e9



From the detailed simulation process and results, the relations between hydraulic cylinder system parameters and performance indexes in time domain when  $Q(S) = 0$  can be easily found as shown in Table 3.

Table 3 The Relations Between Hydraulic Cylinder System Parameters and Performance Indexes in Time Domain when  $Q(S) = 0$

Curve Number		Fig. b)	Fig. c)	Fig. d)	Fig. e)	Fig. f)
		Aleration of $A_1$	Aleration of $m$	Aleration of $V_h$	Aleration of $\omega \lambda_c$	Aleration of $\beta$
1	$\sigma \times 100\%$	191.00	60.50	38.40	11.80	11.80
	$t_s(s)$	0.58	0.542	0.489	0.237	0.237
2	$\sigma \times 100\%$	60.50	112.00	11.80	27.40	21.60
	$t_s(s)$	0.542	0.237	0.237	0.344	0.379
3	$\sigma \times 100\%$	459.00	38.40	81.9	0	7.76
	$t_s(s)$	0.541	0.489	1.19	0.225	0.224

Note: Because of the lack of space, only the overshoot  $\sigma \times 100\%$  and the adjustment time  $t_s$  are listed in the table above.

## Conclusions

The paper created the simulation model of a piston-type hydraulic cylinder, gave its solution, obtained the relation between system parameters and performance indexes of hydraulic cylinder system. These will provide theoretical basis for optimal design of dynamic performance of the hydraulic cylinder. From the results of hydraulic cylinder dynamic simulation above, it is obvious to find this is an effective method to use SIMULINK. This method construct SIMULINK model easily, does not need complex program; it is very intuitive and user-friendly.

The integrated SIMULINK platform based on SIMULINK/MATLAB can combine the advantage of hydraulic technology, control technology and computer technology, and build a supporting platform of collaborative R&D for the mechantronic-hydraulic integrated system. It can deal with modeling, analysis and optimize problems of mechantronic-hydraulic integrated system efficiently, economically and reliably

## References

- [1] Y.T. Li, B.F. Lei and Y.Z. GAO: Hydraulic System Modeling and Simulation(Metallurgy Industry Press, Beijing 2003)
- [2] Katsuhiko: Modern Control Engineering (Third Edition) (Electronics Industry Press, Beijing 2000)
- [3] G.Y. Jiang, Y.Q. Wang and X.C. Yan: Journal of Sichuan University Vol.40(2008)No.5, p.195-198
- [4] Q.H. GAO, X.X. Huang and X.S. Guo: Chinese Mechanical Engineering Vol.14 (2003)No.10, p.823-825.
- [5] S.J. Tian, H. Zhang: Journal of System Simulation Vol.18 (2006)No.5, p.1136-1138,1146.
- [6] H.M. Liang, S.Z. Chen and S.H. You: Computer Simulation Vol.23(2006) No.4, p.241-244,293.

## Study on Formability about ME20M Magnesium Alloy Sheet

Zhang Tingfang<sup>1, a</sup>, Xie Shikun<sup>2, b</sup>

<sup>1</sup>School of Mechanical and Electronic Engineering, Nanchang University, Nanchang 330031, China

<sup>2</sup>School of Engineering, Jingtangshan University, Ji'an, 343009, China

<sup>a</sup>tfzhang@ncu.edu.cn, <sup>b</sup>xskun@163.com

**Keywords:** ME20M magnesium alloy; Formability; Constitutive relationship; Further development

**Abstract.** Warm forming of magnesium alloy sheet has attracted more and more attention in recent years. Mechanics tension test has been made in this paper in order to study the constitutive relationship of ME20M magnesium alloy sheet at different temperatures and strain rates. And a constitutive relationship which includes a softening factor has been put forward. Warm deep drawing experiment and numerical simulation on ME20M magnesium alloy sheet have been made in which the attention was focused on the forming temperature. The results showed that the limit deep drawing height of ME20M magnesium alloy sheet can be dramatically improved as the temperature goes up, especially when the temperature was over about 250° C. Simultaneity, it is feasible and effective to add a material model into numerical simulation software by user subroutine.

### Introduction

Magnesium alloy materials have been received much attention in automotive and electronic industry as the light structural and functional materials in recent years. Sheet metal forming process of magnesium alloy not only meets the demands on the environmental protection and the lighter trend of products, but also can remarkably improve productivity and quantities of the products<sup>[1-4]</sup> with good mechanical performance and surface quality. Deep drawing process is an important and popular process in assessment of formability of sheet metal. So research on magnesium alloy sheet deep drawing is the key technology to acquire complex plastic forming products<sup>[5]</sup>.

At room temperature, magnesium alloy shows poor formability for its hexagonal closed packed structure. It is necessary to enhance the forming temperature so as to improve the formability of magnesium alloys effectively. It has been known that magnesium alloys frequently shows flow softening behavior during deformation at high temperature<sup>[6]</sup>, which increases the difficulty to describe the flow stress behavior of magnesium alloy at high temperature. Numerical simulation is a very effective method to simulate the metal forming process. It can be used not only in the analysis but also in the design to estimate the optimum condition of the forming process. In order to improve the precision in predicting the deformation behavior by numerical simulation, an accurate constitutive relationship about flow stress and strain of magnesium alloy at high temperature need to be researched<sup>[7]</sup>.

The warm deep drawing technology of ME20M magnesium alloy sheet was investigated in this article by both experiment and numerical simulation, and different methods were used to acquire magnesium alloy constitutive relationship in numerical simulation, finally the results from warm deep drawing experiment were compared with that from numerical simulation.

### Constitutive Relationship about Flow Stress of ME20M

The constitutive relationships of the flow stress of a wrought magnesium alloy were researched by some scholars in present studies, but most of those constitutive relationships were deduced based on the hyperbolic sine form to process nonlinearity regression from mechanics tension test data; or to set up coupling constitutive equation based on deformation mechanism, proceeded from density of dislocation and grain size<sup>[8-10]</sup>. These constitutive relationships don't include the main engineering parameters completely and evidently, which may influence practical application in engineering

project. After mechanics tension test of ME20M magnesium alloy sheet was carried out<sup>[11]</sup> at different strain rates and temperatures, and based on the constitutive relationship which was put forward by Dr. Zhang and included a constant softening factor<sup>[7]</sup>, a constitutive relationship which includes an inconstant softening factor and concerns a quantitative relationship among flow stress, strain, strain rate and temperature was brought forward (see Eq. (1)) in this study. It was found by this paper and a great deal of other literatures<sup>[12-14]</sup> that flow softening is more pronounced when strain rate is high and temperature is low. Flow softening is a common characteristic of true stress/true strain curves for many alloys deformed at elevated temperatures. It can be caused by deformation heat and microstructural instabilities inside the deforming material, such as texture formation, dynamic precipitation and dissolution.

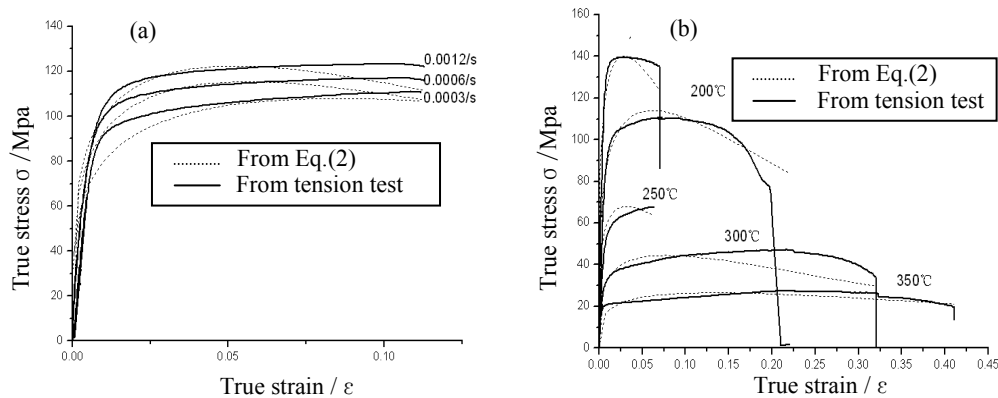
$$\sigma = K \varepsilon^n \dot{\varepsilon}^m \exp(-cT - d * \ln(10000\dot{\varepsilon}) / \ln(T) * \varepsilon) \quad (1)$$

In Eq. (1): 10000 in the inconstant softening factor  $d * \ln(10000\dot{\varepsilon}) / \ln(T)$  is for sake of avoiding a change of sign (from “+” to “-”) of inconstant softening factor when range of strain rates varied greatly (generally from  $10^{-4}$  to  $10^2$ ).

Regression analysis was made from the flow stress/strain values measured in mechanics tension test of ME20M magnesium alloy sheet carried out<sup>[11]</sup> at different strain rates and temperatures. Result was shown as follows:

$$\sigma = 2752.96 \varepsilon^{0.2378} \dot{\varepsilon}^{0.1533} \exp(-0.00677T - 18.443 * \ln(10000\dot{\varepsilon}) / \ln(T) * \varepsilon) \quad (2)$$

As shown in Fig.1, the flow curves forecasted by Eq.2 were compared with that obtained by mechanics tension test at different temperatures and strain rates. They indicate that the accuracy of Eq. 2 is better.



(a) at 200°C but different strain rates      (b) strain rate at 0.0006s-1 but different temperatures

Fig.1 Flow stress/strain curve

### Numerical Simulation on Warm Deep Drawing Technology about ME20M

**The Constitutive Relationship Obtained by the Data From Mechanics Tension Test.** The finite element model, as shown in Fig.2, is established according to the dimensions which are used in the deep drawing experiment. The blank is assumed as a deformable body. The punch, die and blank holder are assumed to be rigid bodies. The thickness of ME20M sheet metal is 3mm.

In the numerical simulation, the constitutive relationship was input from the menu “property” module in ABAQUS/CAE, and its values come from mechanics tension test, the interface is shown in Fig.3. This method only can acquire ME20M constitutive relationship once at a temperature and strain rate, when temperature or strain rate changes, the stress or strain also changes; they have to be input once again, so it is not a good method to build constitutive relationship.

When blank holder force (BHF) is 1KN, friction coefficient is 0.1, the influence of temperatures on limit deep draw height were studied as shown in Fig.4 (a).

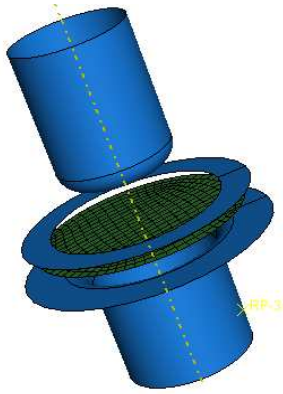


Fig.2 FEA model established in ABAQUS/CAE

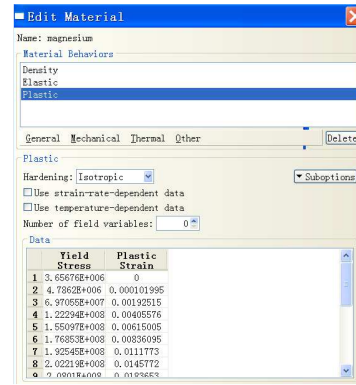
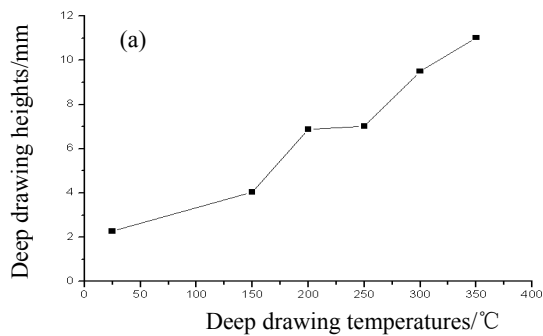
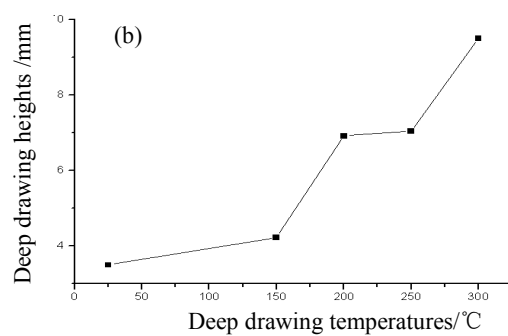


Fig.3 Interface of inputting parameters about constitutive relationship in ABAQUS/CAE



(a) The constitutive relationship obtained by the data from mechanics tension test



(b) The constitutive relationship obtained by user subroutine

Fig.4 Curve of limit deep drawing heights at different temperatures

The limit deep drawing height increases with the temperature goes up, especially when temperature is over about 250°C, It indicates that plastic deforming performance of magnesium alloy becomes better when the temperature rises. Less workable characteristics of magnesium alloy at room temperature is due to the crystal structure of the hexagonal close-packed lattice and only base level {0001} come into slippage. But when temperature is above 200°C, first class pyramid face also begin to slip, so plastic deforming performance increases evidently; when temperature is above 225°C, second pyramid face possibly begin to slip too, so plastic deforming performance increases greatly.

**The Constitutive Relationship Obtained by User Subroutine.** The constitutive equation put forward by this paper (see Eq.2) was added into ABAQUS through further development by user subroutine VUMAT using FORTRAN language.

In ABAQUS/CAE, to establish a complete job and to submit it will create a command file(\*.inp) which can run directly. So some useful sentences or commands (such as constitutive relationship) can be added into the command file. During numerical simulation, the constitutive relationship of ME20M decided by Eq.(2) can be added into the command file. The sentences are as follows:

\*Material, name=magnesium

\*Density

0.00178,

\*USER MATERIAL, CONSTANTS=8 (eight material parameters, E, v, k, n, m, c, d, T)

E, v, k, n, m, c, d, T

In ABAQUS/COMMAND, using command as follows can call files (\*.inp, \*.for) to finish a job.

Abaqus job=\*.inp user=\*.for interactive

Using this method to obtain constitutive relationship, under the same numerical simulation conditions as 3.1, the influence of temperatures on limit deep drawing height was also studied; result was shown in Fig.4 (b). The result was similar with that in Fig.4 (a).

When a parameter such as temperature changes, it only needs to modify its value in \*.inp file, then the relation between stress and strain will change accordingly. So through further development by user subroutine to obtain constitutive relationship is adaptive to realize parameterized finite element analysis (PFEA)<sup>[15]</sup>.

**Experimental Study on Warm Deep Drawing Technology about ME20M<sup>[16]</sup>**

To validate the correctness of numerical simulations (shown in Fig.4), warm deep drawing experiments at different temperature were made. The equipment was shown in Fig.5, the outer diameter of punch is 40mm and radius of its corner is 4mm, the inside diameter of die is 46.6, and the radius of its corner is 6mm. The result was shown in Fig.6; it is very similar as the result of numerical simulation.



Fig.5 Total assembly and mould diagram of warm deep drawing

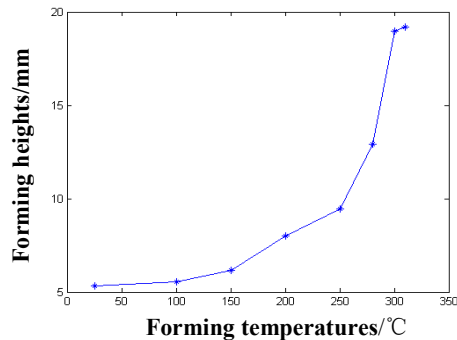


Fig.6 Curve of limit deep drawing heights at different temperatures from

**Comparisons and Analysis**

Limit deep drawing heights influenced by the temperature were listed in Tab.1, which were obtained by numerical simulations (as shown in Fig.4) and deep drawing experiment (shown in Fig.6).

1) The limit deep drawing heights under different temperature obtained by warm deep drawing experiments are greater than those obtained by numerical simulation, but their change trend are accordant. The differences exist because the warm deep drawing experimental result was obtained when cups had been ruptured while results from numerical simulation were obtained when the material only began to be damaged; and during numerical simulation, the forming velocities are greater than those in warm deep drawing experiment in order to shorten calculation time, and other conditions in numerical simulation are impossible the same as those in deep drawing experiment completely.

Table 1 Datasheet of limit deep drawing heights influenced by temperatures

Height(mm) Condition Temperature(°C)	Results from numerical simulation shown in Fig.4(a)	Results from numerical simulation shown in Fig.4(b)	Results of experiment shown in Fig.6
350	14.93	11.025	—
300	10.89	9.503	15.98
250	7.036	7.018	9.47
200	6.917	6.876	7.99
150	4.225	5.786	6.17
Room temperature	3.1	5.090	5.33

2)The limit deep drawing heights of numerical simulation shown in Fig.4(b) are less than those of numerical simulation shown in Fig.4(a) when temperature are over than 150°C, because the former constitutive relationship considered the soften effect at high temperature, the result has greater security in engineering applications than the latter.